J. Non-Newtonian Fluid Mech. 161 (2009) 48–59

Contents lists available at ScienceDirect

Journal of Non-Newtonian Fluid Mechanics

journal homepage: www.elsevier.com/locate/jnnfm

Flow of linear molecules through a 4:1:4 contraction–expansion using non-equilibrium molecular dynamics: Extensional rheology and pressure drop

J. Castillo-Tejas[a,*], A. Rojas-Morales[a], F. López-Medina[a], Juan F.J. Alvarado[c], G. Luna-Bárcenas[d], F. Bautista[e], O. Manero[b]

[a] Facultad de Ciencias Básicas, Ingeniería y Tecnología, Universidad Autónoma de Tlaxcala, Calzada Apizaquito S/N, Apizaco, Tlaxcala, 90300, Mexico
[b] Instituto de Investigaciones en Materiales, Universidad Nacional Autónoma de México, Ciudad Universitaria, México, D.F., 04510, Mexico
[c] Departamento de Ingeniería Química, Instituto Tecnológico de Celaya, Avenida Tecnológico y García Cubas S/N, Celaya, Guanajuato, 38010, Mexico
[d] Centro de Investigación y Estudios Avanzados del Instituto Politécnico Nacional, Unidad Querétaro, Libramiento Norponiente No. 2000, Real de Juriquilla, Querétaro, Querétaro, 76230, Mexico
[e] Departamento de Ingeniería Química CUCEI, Universidad de Guadalajara, Boulevard M. García Barragán No. 1451, Guadalajara, Jalisco, 44430, Mexico

ARTICLE INFO

Article history:
Received 19 September 2007
Received in revised form 13 March 2008
Accepted 17 April 2009

Keywords:
Non-equilibrium molecular dynamics
Extensional rheology
Pressure drop

ABSTRACT

In this work, non-equilibrium molecular dynamics simulations are used to generate the flow of linear polymer chains (monomer-springs with FENE potential) and a Lennard–Jones fluid (Newtonian fluid) through a contraction–expansion (4:1:4) geometry. An external force field simulating a constant pressure gradient upstream the contraction region induces the flow, where the confining action of the walls is represented by a Lennard–Jones potential. The equations of motion are solved through a multiple-step integration algorithm coupled to a Nosé-Hoover dynamics [S. Nose, A unified formulation of the constant temperature molecular dynamics methods, J. Chem. Phys. 81 (1984) 511–519], i.e., to simulate a thermostat, which maintains a constant temperature. In this investigation, we assume that the energy removed by the thermostat is related to the viscous dissipation along the contraction–expansion geometry. A nonlinear increasing function between the pressure drop and the mean velocity along the contraction for the linear molecules is found, being an order of magnitude larger than that predicted for the Lennard–Jones fluid. The pressure drop of both systems (the linear molecules and Lennard–Jones fluid) is related to the dissipated energy at the contraction entry. The large deformation that the linear molecules experience and the evolution of the normal stress at the contraction entry follow a different trajectory in the relaxation process past the contraction, generating large hysteresis loops. The area enclosed by these cycles is related to the dissipated energy. Large shear stresses developed near the re-entrant corners as well as the vortex formation, dependent on the Deborah number, are also predicted at the exit of the contraction. To our knowledge, for the first time, the excessive pressure losses found in experimental contraction flows can be explained theoretically.

1. Introduction

A notorious benchmark problem in rheology has been the prediction of the dissipation and its relation with the pressure drop along flow trajectories that involve abrupt changes in geometry. In particular, the viscoelastic flow through a contraction, or contraction–expansion geometries, has been given special attention as a test to current constitutive equations. Complex flows experience an unusual large pressure drop along the contraction as compared to that corresponding to a Newtonian fluid with similar viscosity. Large shear stresses develop near the re-entrant corner regions while similarly large extensional stresses are generated along the central streamline of the flow domain. Vortex generation and large molecular deformation are observed in the flow patterns along the geometry. Birefringence measurements reveal high anisotropy at the entry region of the contraction followed by a relaxation to an isotropic state at the exit. However, a standing problem has been the prediction of the pressure drop along the contraction geometry and its relation with the dissipation processes occurring along the flow trajectory. Furthermore, analyses of the stress and conformation along the flow trajectory have pointed out the presence of hysteresis cycles along the entry and exit regions of the flow domain. Yet, the relationship existing between the pressure drop predictions and the hysteresis cycles

* Corresponding author. Tel.: +52 241 41 72544; fax: +52 241 41 75844.
E-mail address: j_castillo_tejas@hotmail.com (J. Castillo-Tejas).

0377-0257/$ – see front matter © 2009 Elsevier B.V. All rights reserved.
doi:10.1016/j.jnnfm.2009.04.005

is still not clear. In this work, we analyze the pressure drop, conformation hysteresis and the dissipation process along the contraction–expansion region, for various values of the Deborah number, with non-equilibrium molecular dynamics simulations.

Several explanations have been given to the excess pressure drop in viscoelastic liquids undergoing complex flow situations. The existence of stress-conformation hysteresis cycles is assumed to be closely related to the dissipation process occurring in these flows. Doyle et al. [1] found a stress-conformation hysteresis in uniaxial extension. Theoretical predictions of the hysteretic cycles were made using Brownian dynamics applied to several dumbbell models and to the bead-rod chain. A relevant result shows that very small changes in the chain conformation can result in very large changes in the stress. The evolution of stress and birefringence in the initial deformation process follows a path which is different to that observed in the subsequent relaxation process. The hysteresis observed in some of the models is in qualitative agreement with experiments involving polystyrene and poly-isobutylene-based Boger fluids.

Lielens et al. [2] performed stochastic simulations in one-dimensional elongational flows using the simple FENE model translated into an equivalent macroscopic constitutive equation, predicting hysteretic behavior. Sizaire et al. [3] further discussed the hysteretic behavior of dilute polymer solutions in relaxation following extensional flow, adopting the theoretical framework of FENE dumbbells and related macroscopic constitutive equations. Conclusions show that the hysteretic behavior results from the combined effect of variation in the distribution of individual configurations and non-linearity in the dumbbell model.

Rothstein and McKinley [4–7] analyzed the flow of a Boger fluid through a 4:1:4 contraction/expansion. For high Deborah numbers an elastic instability is found, which is not directly connected to the excess pressure drop or to the re-entrant corner curvature. Rather, this is assumed to be originated by dissipation associated to the stress-conformation cycles. An excess pressure drop above the Newtonian reference is found, independent of the contraction ratio and curvature of the contraction entry. In polystyrene solutions for $De > 0.5$, the dilute solution exhibits a marked hysteresis cycle that is not present in more concentrated solutions. Beyond a critical De number, the hysteresis cycles and the dissipated energy are closely related to the pressure drop, provided that the uniform transient uniaxial elongational flow can simulate the centre-line stresses and molecular conformations existing in the contraction flow. Under these premises, the area enclosed in the hysteretic loops is shown to be proportional to the dissipated energy of the deformation history.

Additional experimental works also have found excess pressure drops above the Newtonian reference fluid. Nigen and Walters [8] found an excess pressure drop in Boger fluids higher than that measured in Newtonian fluids in axisymmetric contractions, but not in the planar cases. Schroeder et al. [9] analyzed the extensional flow of DNA molecules using fluorescence microscopy. The hysteresis cycles found are assumed to be originated from hydrodynamic forces and may directly influence bulk-solution stresses and the development of stress–strain relations in dilute polymer solutions.

Additional numerical simulation contributions are numerous [10–15,18–23] as well as the constitutive equations used to reproduce the kinematics and dynamics of the contraction–expansion flow. Using a constitutive equation derived from the FENE model, Szabo et al. [10] simulated a flow through a 4:1:4 contraction–expansion. They found an increase in the vortex size at the contraction entry with De number. Results of the pressure drop, however, show a decrease with respect to the Newtonian reference liquid, except when the extensibility parameter is small. Binding et al. [13] in a contraction–expansion flow the pressure gradient on the centre-line shifts downstream as the Deborah number is increased and the peak value of the pressure gradient decreases. Similar results are found by Aguayo et al. [14] using an Oldroyd-B equation through planar and axisymmetric contraction and contraction–expansion geometries. Wapperom and Keunings [15] used the Pom-Pom model [16,17] through a 4:1:4 contraction–expansion with rounded corners found an increase in the vortex size with De number, but again a decrease in the pressure drop with respect to the Newtonian reference liquid, in contrast to experimental results. Alves et al. [18,19] simulated a viscoelastic flow through a 4:1 contraction using the Oldroyd-B and PTT models observing the vortex inhibition with increasing De. In Boger fluids the vortex size was found to follow a non-monotonic behavior with the flow rate.

It is apparent that numerical simulations face a difficulty in describing the experimental data through a contraction, particularly the pressure drop. This problem arises in the context of the need to more advanced solution methodologies and appropriate constitutive equations that include accurate descriptions of the dissipation process occurring in the flow domain, to predict more adequately the dynamics of polymer solutions through complex geometries. In this regard, predictions from continuum models complemented with those of more molecularly oriented models are necessary to grasp some of the fundamental problems related with the dissipation occurring in the flow through complex geometries.

Theoretical developments and simulations of complex liquids flowing through abrupt changes in geometry include those based on continuum mechanics, Brownian dynamics and molecular dynamics. They differ in the particular simulation scale, namely, 10^{-3} m for continuum models, 10^{-6} m for *Coarse-Grained* models used in Brownian dynamics simulations (which do not describe specific details at the atom level) and 10^{-9} m for molecular dynamics at the microscopic level. The latter has been shown to predict the response of polymeric materials, in qualitative agreement with continuum simulations [24]. Here we use molecular dynamics to simulate the flow of molecules along complex geometries. It is expected that this approach is able to describe the response of the fluid to such abrupt changes in geometry, although the simulation scale is not comparable to macroscopic predictions from continuum models. However, the qualitative agreement of both approaches is encouraging and justifies molecular simulations.

Previous studies on molecular models include the analysis by Todd et al. [25] using a Lennard–Jones fluid with periodic boundary conditions in the three directions, and Mi and Chwang [26] using molecular dynamics to simulate the Poiseuille flow along nanochannels of various shapes. Using molecular dynamics simulations, Castillo-Tejas et al. [27] analyzed the instabilities found in Poiseuille flow of systems of linear and branched chains with various wall interactions, and attention was given to the influence of the wall surface on slip and molecular deformation of the material.

Homogeneous extensional flow presents difficulties for non-equilibrium molecular dynamics simulations, since the results are dependent on the size of the simulation domain in the normal direction to flow [28]. In planar extensional flow, Todd and Daivis [29] suggest the modification of the periodic boundary conditions to obtain mean values of the off-diagonal components of the stress tensor and also extensional viscosity predictions.

The present work aims to analyze the flow of a polymer modeled as monomer-springs with a FENE potential through a 4:1:4 contraction–expansion geometry and compare it with the Newtonian fluid (modeled as a Lennard–Jones fluid), with non-equilibrium molecular dynamics simulations. Special attention is given here to the phenomena associated to the excess pressure drop and its relationship with the stress-conformation hysteresis cycles previously discussed. As it is shown below, large increases of the pressure drop of the polymer as compared to those of the New-

tonian fluid are predicted, and explanations of the origin of these pressure losses are given for the first time.

The manuscript is organized as follows. Section 2 presents the molecular model and the equations of motion to simulate the flow. Section 3 examines the simulation domain, the rheological properties calculations and technical details of the simulations. Section 4 discusses the flow of the two systems, the linear chains (polymer) and the Lennard–Jones (Newtonian fluid), and shows results of extensional flow, including the pressure drops through the geometry. An analysis of the structural changes is provided as functions of the Deborah number and their relations with the flow properties. Finally, in Section 5, discussion and the main conclusions are presented.

2. Theoretical

2.1. Equations of motion

In Poiseuille flow, the motion is produced by a pressure gradient along the flow direction. In molecular dynamics the flow motion is simulated by an external force F_e which ensures that the system maintains longitudinal homogeneity [25,30]. The Poiseuille flow simulations require that the particle motion is described by the Newtonian equations of motion,

$$\frac{d\mathbf{r}_i}{dt} = \mathbf{v}_i \tag{1}$$

$$\frac{d\mathbf{v}_i}{dt} = \frac{\mathbf{F}_i}{m_i} + \frac{F_e}{m_i}\mathbf{i} - V_\xi \mathbf{v}_i \tag{2}$$

$$\frac{d\xi}{dt} = V_\xi \tag{3}$$

$$\frac{dV_\xi}{dt} = \frac{1}{Q_S}\left[\sum_i m_i v_i{}^2 - \frac{L_S}{\beta}\right] \tag{4}$$

where $\mathbf{r}_i$ is the position vector, $\boldsymbol{i}$ is a unit vector placed along the flow direction and F_e is the magnitude of the external force field which maintains the flow. $\mathbf{F}_i$ acts upon each monomer of mass m_i and it is related to fluid–fluid and fluid–wall interaction forces. Vector $\mathbf{v}_i$ represents the velocity of particle i in the *laboratory* frame of reference, namely, the sum of the peculiar velocity and the streaming velocity. The peculiar velocity is the rate of change of the position of the particle under equilibrium conditions, i.e., in absence of external perturbations. According to the geometry under study, only the y-component of the velocity vector develops a peculiar velocity.

The flow itself generates heat which needs to be removed from the system. The Nose–Hoover [31] thermostat is here used to maintain the temperature constant, where its dynamic variables ξ and V_ξ are the coordinates of position and velocity, respectively, and Q_S is its associated mass. Finally, L_S is the degree of freedom and β is the reciprocal of the reduced temperature.

In this work, specifically, is important to obtain the energy amount that the thermostat removes from the dynamic variables. Solution of Eqs. (1)–(4) allows obtaining the position vector and laboratory reference velocity ($\mathbf{r}_i$ and $\mathbf{v}_i$) according to the constant simulation conditions N, V and T. As the temperature depends on molecular velocity, the thermostat removes or introduces heat which in turn affects the particle velocities. The force to maintain the temperature constant is given by the third term of the right-hand-side of Eq. (2), expressed as the gradient of a potential (see Eq. (12)) as follows:

$$\frac{d}{d\mathbf{r}_i}U_{NHi} = V_\xi m_i \mathbf{v}_i \tag{5}$$

Here U_{NHi} is the energy removed by the thermostat for particle i. Eq. (5) is in turn derived with respect to time to obtain:

$$\frac{dU_{NHi}}{dt} = V_\xi m_i v_i^2 \tag{6}$$

Using the Liouville operator formulation, Eq. (6) is in turn integrated according to the following transformation [32]:

$$U_{NHi} \to U_{NHi} + \frac{\Delta t}{2} m_i V_\xi v_i^2 \tag{7}$$

Eq. (7) represents the energy $U_{NH} = \sum_{i=1}^{N} U_{NHi}$ that the thermostat removes in the whole system and it is used to estimate the rate of energy removed by thermostat.

To maintain longitudinal homogeneity in the system, the Poiseuille flow is generated by a force F_e applied on the particles. However, since the flow past contraction–expansion geometry is not homogeneous in the flow direction, F_e is applied only at the simulation entry region, $x_1 < x < x_2$ as shown in Fig. 1. The expression for the external force is:

$$F_e(x_i) = a - \frac{a(x_i - c)^2}{b} \tag{8}$$

where a is the magnitude of F_e, x_i is the x-component of the position of the particle i, $c = (x_1 + x_2)/2$ and $b = (x_2 - x_1)^2/4$, with $x_1 = -90.92\sigma$ and $x_2 = -79.55\sigma$. The external field F_e is zero on x_1 and x_2, such that the field is consistent with the concept of minimum image and periodic boundary conditions along the flow direction. To determine the energy U_{F_e} associated to F_e, an analogous procedure to that for $\sum_{i=1}^{N} U_{NHi}$ is followed, such that

$$U_{F_e} = -ax_i + \frac{a(x_i - c)^3}{3b} + c_2 \tag{9}$$

where c_2 is the integration constant. Finally, the potential energy of the system resulting from the application of the external force is given by:

$$U(\mathbf{r}^N, \xi, V_\xi) = \sum_{i=1}^{N} U_{Fe}(\mathbf{r}_i \cdot \mathbf{i}) + \sum_{i}^{N}\sum_{i<j}^{N-1} U(\mathbf{r}_i, \mathbf{r}_j) + \sum_{i=1}^{N} U_{NH_i} \tag{10}$$

The system of equations is solved through a reversible integration algorithm *RESPA* (*Reversible Reference System Propagator Algorithm*) [32,33], where the motion established by the Liouville propagator for the thermostat dynamic variables occurs within the same scale of the reference system [34].

2.2. Molecular model

In molecular dynamics formulations, the motion of particles in the system is described by classical mechanics including particle–particle interactions. The detailed interaction among particles is given by summation of the overall pair–pair contributions according to:

$$U(\mathbf{r}^N) = \sum_i \sum_{j>i} U(r_{ij}) \tag{11}$$

where $U(r_{ij})$ accounts for the potential energy among pairs and r_{ij} is the scalar distance between particles i and j. The force acting on a particle is obtained from the gradient of the potential function:

$$\mathbf{F}_i = -\frac{\partial U(\mathbf{r}^N)}{\partial \mathbf{r}_i} \tag{12}$$

In this work, the systems are: (1) molecules of linear chains and (2) Lennard–Jones soft spheres. A linear molecule is represented here according to the monomer-spring model of Kremer and Grest [35]. This model considers that the polymer chain formed by a

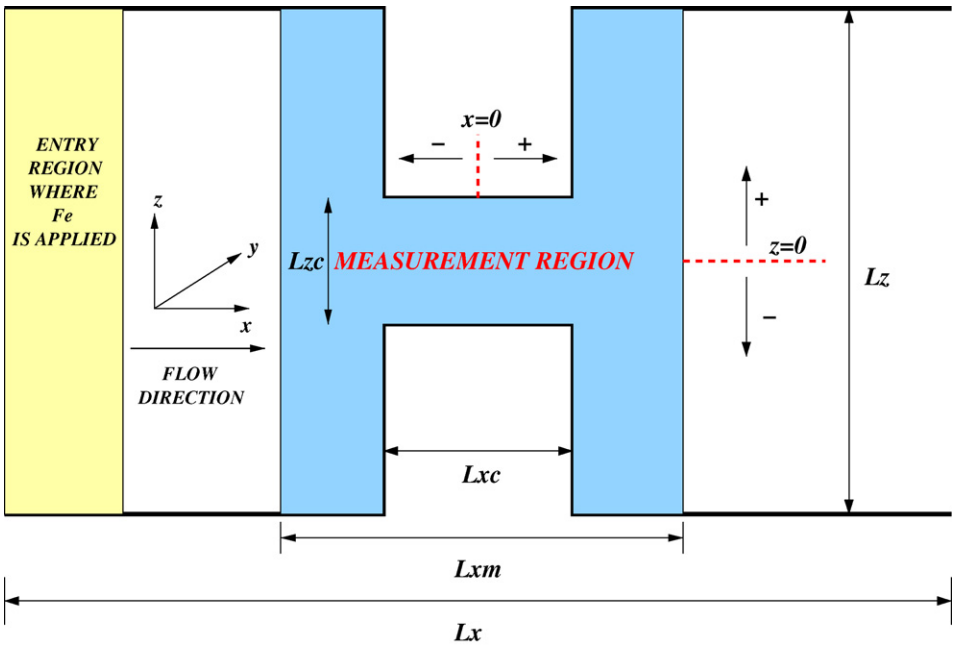

Fig. 1. Schematic representation of the simulation region for the 4:1:4 contraction–expansion flow.

wealth of particles is replaced by a spring and the mass is concentrated in a monomer or segment. Then, a chain is envisaged as a collection of segments connected through non-harmonic springs. According to this model, the functional form of the intermolecular potential $U(\mathbf{r}^N)$ includes two types of interactions among the segments of linear molecules: bonding and non-bonding interactions. The non-bonding interactions are of the van-der-Waals type, such that the interaction energy between two segments is the truncated Lennard–Jones pair potential, smoothed at a cut-off distance of $r_c = 2^{1/6}\sigma$,

$$U_{LJ} = \begin{cases} 4\varepsilon\left[\left(\dfrac{\sigma}{r_{ij}}\right)^{12} - \left(\dfrac{\sigma}{r_{ij}}\right)^{6}\right] - \Delta\Phi, & r_{ij} < r_c \\ 0, & r_{ij} \geq r_c \end{cases} \tag{13}$$

where r_{ij} is the scalar distance between segments i and j, and σ and ε are the collision diameter and potential depth, respectively, and $\Delta\Phi$ is a shifting parameter. In this work we neglect particle–particle interactions whose separation is larger than the cut-off radius r_c. The term $\Delta\Phi$ removes the discontinuity in the energy at $r_{ij} = r_c$. The non-bonding interactions are described by a short-range repulsive potential, the Weeks–Chandler–Andersen (WCA) potential [36]. At the density conditions considered, the repulsive interactions are predominantly responsible of the structure behavior of the system.

The bonding interactions arise between two segments joined by covalent bonds. A finite-extensible non-linear elastic (FENE) potential [37] is used to model adjacent segments connectivity in the same molecule, and it is given by

$$U_{\text{FENE}} = \begin{cases} -\dfrac{k_v {R_0}^2}{2} \ln\left[1 - \left(\dfrac{r_{ij}}{R_0}\right)^2\right], & r_{ij} < R_0 \\ \infty, & r_{ij} \geq R_0 \end{cases} \tag{14}$$

where k_v is the spring constant ($k_v = 100$) and R_0 (=1.5) is the maximum extension of the bond. The attractive FENE potential reproduces conveniently the behavior of polymer solutions [38]. The monomer-spring model has been used in molecular dynamics simulations in confined polymer system [39,40]. Recently, with the same potential instabilities in the Poiseuille flow of polymer melts were analyzed [27]. Variations of the FENE potential have also been used in systems with attractive walls and a Morse potential for non-bonding interactions [41]. It is important to mention that the FENE potential is used here to model the attractive force and does not imply a constitutive expression for the stress.

Finally, the Newtonian fluid is represented by Lennard–Jones soft spheres, where the interactions between particles are given by Eq. (13). For monomer–wall and L–J particle–wall interactions, it is considered that the wall is made of Lennard–Jones particles.

3. Technical details

3.1. Reduced properties

The system variables are expressed in terms of reduced quantities with respect to the mass (m_i), energy (ε) and length (σ), to which a value of one is assigned. This formulation presents an advantage, namely, that the principle of corresponding states can be applied. [42].

The mass is expressed in units of atomic mass, the energy is given in units of the depth of the well potential and the lengths are referred to the particle diameter. The reduced expressions of some properties are listed below [43]:

$$\rho^* = \rho\sigma^3, \qquad T^* = \frac{k_B T}{\varepsilon}, \qquad U^* = \frac{U}{\varepsilon}, \qquad \mathbf{P}^* = \frac{\mathbf{P}\sigma^3}{\varepsilon},$$

$$t^* = t\left(\frac{\varepsilon}{m\sigma^2}\right)^{1/2}, \qquad \dot{\gamma}^* = \left(\frac{m\sigma^2}{\varepsilon}\right)^{1/2} \dot{\gamma} \text{ and } \eta^* = \left(\frac{\sigma^4}{m\varepsilon}\right)^{1/2} \eta,$$

where ρ is the local density, k_B is the Boltzmann constant, U is the energy, $\mathbf{P}$ is the stress tensor and t is time. Results are expressed in reduced units with no extra signals.

3.2. Geometry and simulation conditions

The particles are confined in a simulation region shown in Fig. 1. Dimensions are given in units of σ of a computational region with a 4:1:4 contraction–expansion ratio where the origin is located in the middle point of the domain. The minimum image and periodic boundary conditions impose equal values of the transport and

structural properties of the fluid at the entry and exit regions. The following situations are then applied: (1) L_{xc} is equal to the maximum length of the extended chain, (2) L_x should be sufficiently large as to avoid that the boundary conditions in the x-direction affect the flow, and then L_x is fixed to $13L_{xc}$, (3) L_{zc} is such that the contraction confinement allows reproducing bulk situations [27], (4) $L_z = 4L_{zc}$ and finally, (5) $L_y = 2r_c$, where r_c is the cut-off radius of the intermolecular potential. On this basis, the position coordinates domain is the following:

$$-90.92\sigma < x < 90.92\sigma, \quad -1.73\sigma < y < 1.73\sigma \quad \text{and}$$

$$-21.738\sigma < z < 21.738\sigma,$$

where the contraction itself is located at: $-6.9935\sigma < x < 6.9935\sigma$ and $-5.4345\sigma < z < 5.4345\sigma$.

Notice that the measurement region is limited to the range $-45.46\sigma < x < 45.46\sigma$, as shown in Fig. 1. To simulate the confinement effect, a Lennard–Jones surface is placed at the boundaries of the simulation domain. The minimum image and periodic boundary conditions are then applied to the flow and neutral directions, respectively. If the centre of mass of a chain leaves the simulation domain along the x and y directions, the chain enters the region through the opposing side.

As mentioned in Section 2.1, F_e is applied to each particle positioned at the entry point of the simulation domain $-90.22 < x < -79.55$ as shown in Fig. 1. To maintain longitudinal homogeneity, the external force is applied to all particles, as reported in other simulation works. However, the contraction flow is not homogeneous, so F_e is imposed only at the entry region of the simulation domain. Therefore, the flow is developed at the entry region and the test region is not directly affected.

The system with linear chains contains 1666 chains, each one containing 13 monomers of size σ connected themselves, such as the particle number N is 21,658. The same size is used for the Lennard–Jones fluid. Additionally, the reduced temperature and density are 4 and 0.84, respectively.

The magnitude of the external force F_e is varied between 0.5 and 3 for linear chains and from 0.125 to 1.0 for L–J soft spheres. The initial configuration of particles is generated considering that the entire simulation domain is composed of multiple sub-domains with the following dimensions: $L_x = 13\sigma$, $L_y = 3.46\sigma$ and $L_z = 10.869\sigma$. Particles lying in this region are equilibrated in absence of external perturbations and replicated along the entire domain. Once the initial configuration is generated, the external force is imposed to produce the flow. The integration steps amount to 2 million, from which one million steps are required for equilibrium conditions. A time step of $\Delta t = 0.001$ is set to integrate the equations of motion using the reversible *RESPA* algorithm developed from the Liouville propagator.

3.3. Calculation of the system properties

3.3.1. Radius of gyration R_g

Conformations of linear chains for various simulation conditions are analyzed by calculating the mean-squared radius of gyration $\langle R_g^2 \rangle$, which allows obtaining the global distribution of the chain segments:

$$\langle {R_g}^2 \rangle = \frac{1}{E_l} \left\langle \sum_{i=1}^{El} (\mathbf{r}_i - \mathbf{r}_m)^2 \right\rangle \tag{15}$$

$\mathbf{r}_m$ is the center of mass of the chain and E_l is the number of segments per chain. The radius of gyration can also be obtained by summing the three eigenvalues (I_x, I_y, I_z) representing the three main axes of the ellipsoid (containing the segment distribution in the three directions) of the mass distribution tensor $\mathbf{G}$.

3.3.2. Viscous dissipation E_v

The expression for the viscous dissipation integrated over the entire system volume is given by

$$E_v = -\int (\boldsymbol{\tau} : \nabla \mathbf{v}) dV \tag{16}$$

where $\boldsymbol{\tau}$ is the viscous stress tensor and $\nabla \mathbf{v}$ is the velocity gradient. Here the rate of viscous dissipation is assumed, as a first approximation, to be equal to the rate of energy amount that the thermostat removes to maintain a constant temperature, such that

$$E_v \approx \frac{\left\langle \sum U_{NHi}|_{t+\Delta t} - \sum U_{NHi}|_t \right\rangle}{\Delta t} = \frac{\Delta U_{NH}}{\Delta t} \tag{17}$$

The validity of Eq. (17) is analyzed in Section 4.2 below.

3.3.3. Stress tensor

In this work, the plane method for non-homogeneous flow is used [25,44] to calculate the pressure tensor in the fluid, according to the following expression:

$$P_{\beta\alpha}(\beta) = \frac{1}{A} \left\langle \sum_{i=1}^{N} \frac{p_{\alpha i} p_{\beta i}}{m_i} \delta(\beta - \beta_i) \right\rangle + \frac{1}{2A} \left\langle \sum_{i=1}^{N} F_{\alpha i} \ \mathrm{sgn}(\beta_i - \beta) \right\rangle \tag{18}$$

where $P_{\beta\alpha}$ is the pressure tensor component acting along direction α through a plane normal to the β axis. A is the area of the plane normal to the β axis, $\mathrm{sgn}(\beta_i - \beta)$ is equal to one if $(\beta i - \beta) > 0$ and to -1 if $(\beta_i - \beta) < 0$. Moreover, $F_{\alpha i}$ is the α-component of the force acting on particle i, and $p_{\alpha i}$ and $p_{\beta i}$ are the α and β components of the momentum of particle i, respectively. The stress tensor $\mathbf{T}$ is related to the non-equilibrium components of the pressure tensor such that $\mathbf{T} = -\mathbf{P}$. The total stress $\mathbf{T}$ implies the contribution of the pressure and that of the viscous stress, such that $\mathbf{T} = -p\mathbf{I} + \boldsymbol{\tau}$. The plane method allows calculating the stress components T_{xx}, T_{zz} and T_{zx} in the computational domain. In molecular dynamics the total normal stress contains the non-separable contributions from the viscous stress $\boldsymbol{\tau}$ and pressure $-p\mathbf{I}$.

4. Results and discussion

4.1. Simple shear flow

Simulations of the viscoelastic simple shear flow of linear-chain molecules involve 300 molecules, each one containing 13 sites. For the Lennard–Jones fluid, simple shear flow is generated for a system comprising 3000 particles. Same density and temperature conditions of the contraction flow (0.84 and 4, respectively) are used for both systems, with Lees–Edwards periodic boundary conditions [45] coupled to a Nosé–Hoover thermostat to maintain a constant temperature.

Fig. 2 presents the viscosity η for both systems and the first normal-stress difference N_1 as functions of the shear rate γ in simple shear flow. For the linear molecules, at low shear rates the viscosity is constant (first Newtonian region) and as the shear rate increases the viscosity shear thins with a slope about of -0.39, near the range as observed in polymer solutions and melts (0.4–0.9) [46]. The slope is a regression curve of values obtained at several shear rates. In reduced units, the relaxation time λ obtained from the relation $\lambda = \Psi_{1,0}/2\eta_0$ is 17.51, where $\Psi_{1,0}$ and η_0 are the first normal-stress coefficient and the zero-shear rate viscosity, respectively, obtained from the simulations at low shear rates. As the fluid changes from isotropic to anisotropic, N_1 increases with rising molecular deformation along the flow direction. For the Lennard–Jones fluid, the shear viscosity is constant along the range of shear rates presented, and therefore this system represents the Newtonian fluid behavior.

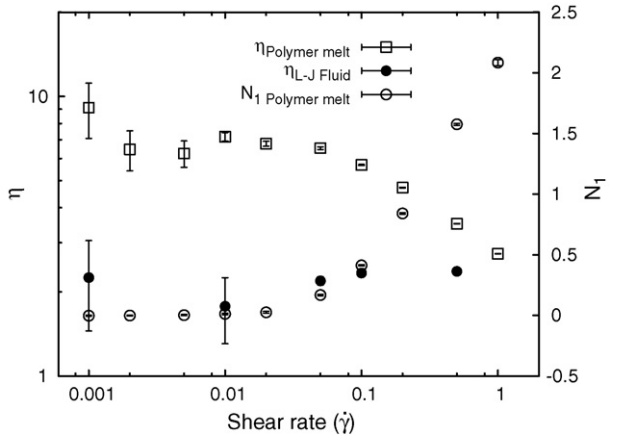

Fig. 2. Shear viscosity and first normal-stress difference as functions of shear rate under simple-shear flow for the linear chain and Lennard–Jones fluids.

4.2. Viscous dissipation and energy removed by the thermostat

The term $-\boldsymbol{\tau} : \nabla \mathbf{v}$, included in Eq. (16), describes the irreversible loss of mechanical energy into thermal energy. In polymeric fluids, viscous dissipation generates an increase in the system temperature and velocity gradients [47]. One of the fundamental assumptions of the present work considers that the increase in temperature by viscous dissipation is associated to an energy content that is equivalent, to a first approximation, to the energy content that the thermostat removes to maintain a constant temperature. For the purpose to demonstrate the basis of this assumption, a steady simple shear is imposed on a system formed by 800 Lennard–Jones soft spheres under same conditions of the flow curve in Fig. 2. In this flow, the position coordinate and *peculiar velocity* coordinate evolve according to SLLOD dynamics [30]. The rate of dissipation for this flow is given by the product of the mean shear stress, the shear rate and the simulation volume, such that $E_v = \langle \tau_{zx} \rangle \dot{\gamma} V$. Fig. 3 presents the variation of the rate of viscous dissipation ($E_v = \langle \tau_{zx} \rangle \dot{\gamma} V$) and the rate of energy removed by the thermostat ($\Delta U_{NHx}/\Delta t$, $\Delta U_{NHy}/\Delta t$, $\Delta U_{NHz}/\Delta t$) as functions of the shear rate for each velocity component. At a shear rate of 0.1, the viscous dissipation is slightly larger than the energies removed by the thermostat. This can be interpreted as an energy amount added to the system by the thermostat. Upon increasing the shear rate, only the rate of energy removed in x-direction tends to be slightly larger than the viscous dissipation. Although the viscous dissipation increases two orders of magnitude for shear rates from 0.1 to 1.0, the difference $\Delta U_{NHy}/\Delta t - E_v$ diminishes as the shear rate increases. This behavior demonstrates the equivalence between the rate of dissipation energy and the rate of energy removed by thermostat for each peculiar velocity component.

When the thermostat is applied to three component of vector velocity, the peculiar velocity distribution is Maxwellian, i.e., it describes a Gaussian with deviation $(k_B T/m)^{1/2}$ and zero mean velocity ($\langle v \rangle = 0$) at a mean temperature ($\langle T \rangle$). By equipartition of kinetic energy, the scalar components of the velocity are mutually independent [48], namely, they exhibit same distribution and deviation. This implies that each peculiar velocity component has the same contribution to the mean temperature and therefore their energy contribution is the same fraction of the total energy removed by the thermostat. On this basis and according to the results in simple shear flow, the rate of energy removed by the thermostat is estimated, for convenience, taking into account the only peculiar velocity component (y-component of the velocity).

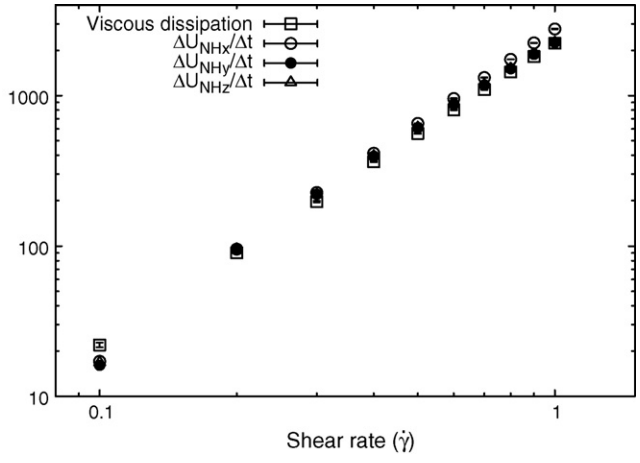

Fig. 3. Rate of viscous dissipation and energy removed by the thermostat as a function of the shear rate.

4.3. Flow through A 4:1:4 contraction–expansion

4.3.1. Extensional flow

This complex flow involves a non-constant deformation along the central streamline. To characterise the change of elastic energy during the deformation-relaxation process, the results are reported in terms of the non-dimensional Deborah number (De), given by $\mathrm{De} = \lambda U/L_{zc}$, where λ is the relaxation time and U is the mean velocity in the contraction region.

Fig. 4 presents the variation of the velocity of the linear molecules $v_x(x)$ along the central streamline for various values of the Deborah number. In this case the central streamline is divided in 200 y–z planes, each one with a height of 2σ and a width of L_y. Notice that the contraction is located in the region $-6.99 < x < 6.99$. Upstream, the molecular velocity $v_x(x)$ is constant up to a distance of $x \approx -30\sigma$. From this point on, velocity increases with De up to a maximum located just at the contraction entrance. For De values of 1.9, 3.9 and 5.5, velocity is near constant in the contraction region and decreases at the exit, just before the expansion. For large De values (6.3, 6.7, and 7.0) the maximum of the fluid velocity shifts to regions downstream the expansion. Consequently, the velocity gradient exhibits two peaks, one located just before the contraction and another one located just at the beginning of the expansion. In the expansion there is a negative peak corresponding to the decrease in the axial velocity. For linear molecules, Fig. 5 shows the velocity gradient variation along the central region prior and in the contraction. At the point where the velocity increases ($x \approx -30\sigma$)

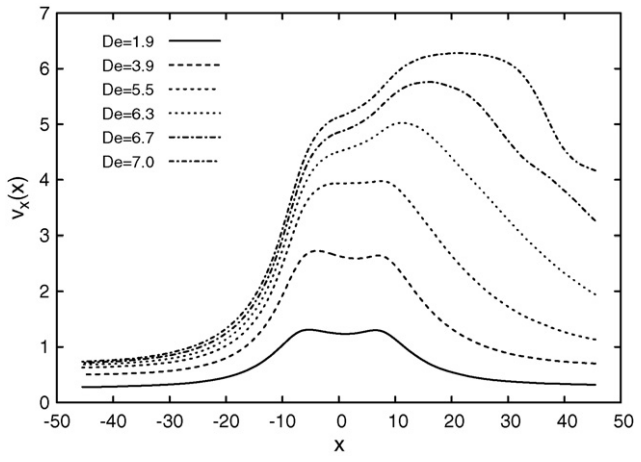

Fig. 4. Centerline velocity along the axial coordinate for various Deborah numbers.

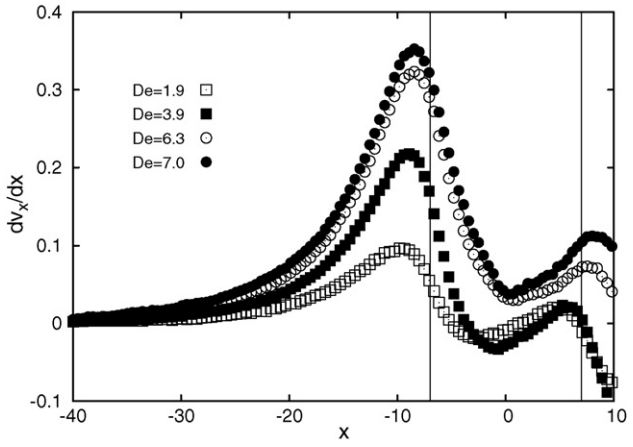

Fig. 5. Axial velocity gradient along the flow direction for various Deborah numbers.

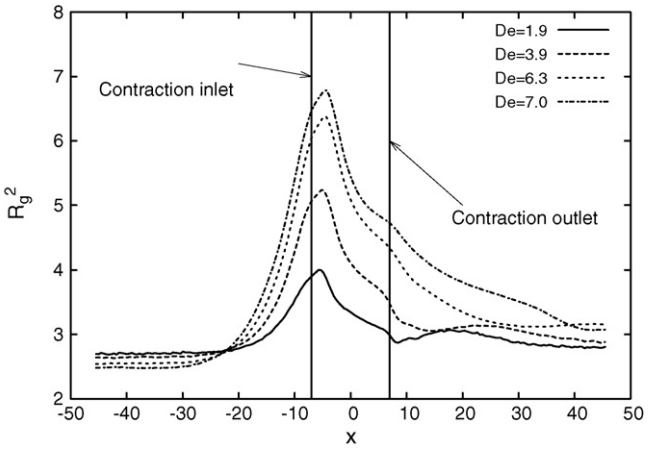

Fig. 7. Radius of gyration along the central streamline for various Deborah numbers.

the fluid experiences an abrupt deformation before entering the contraction, and the magnitude of the maximum depends on the Deborah number. The deformation rate increases with the De number, in agreement with experiments performed by Graham et al. on the contraction flow of monodisperse linear entangled polystyrene melts [49]. Right at the contraction, the strain rate diminishes and attains a second relative maximum in the exit of the contraction. The strain rate describes a minimum (not shown) in the expansion region and eventually levels-off recovering the zero value it had upstream the contraction.

For linear molecules, Fig. 6 describes the variation of N_1 along the central streamline. Upstream the contraction, the first stress difference presents positive values up to $x \approx -22\sigma$, due to the large extensional stress. The normal-stress difference changes sign as the contraction is approached due to the diminishing extensional stress and the increase in the normal stress. The normal stress increases drastically with Deborah number, as the fluid approaches the contraction region, resulting in a peak in the negative value of N_1. Inside the contraction, the normal-stress difference starts its relaxation process as the tension on the molecules relaxes. The increase in the normal-stress component as the contraction is approached is related to the increase in the pressure drop, similarly to the increase in the velocity gradient prior to the contraction region.

The increase in the normal stress as the contraction is approached suggests substantial changes in the molecular deformation. Fig. 7 shows the radius of gyration R_g^2 along the centerline of the geometry. Upstream the contraction R_g^2 remains constant up to a distance $x \approx -22\sigma$, where deformation of the molecule in the flow direction starts to increase up to a maximum at the contraction itself. Those molecules subjected to larger Deborah numbers deform more. Past the contraction the molecule relaxes as the expansion is approached. Upstream the 4:1:4 contraction–expansion device, the molecule is deformed and oriented along the flow direction followed by a fast relaxation process past the contraction [4–7].

Fig. 8 presents the components I_x^2 and I_z^2 of the radius of gyration along the central region corresponding to De = 7.0. The peak in the component of the radius of gyration along the flow direction almost coincides with the peak in the strain rate shown in Fig. 5. The maximum deformation along the flow direction at the onset of the contraction coincides with a compression along the normal direction. These results are in agreement with the chain anisotropy data along the contraction expansion by Graham et al. [49] in linear monodisperse entangled polymers. Due to the strong elongational component of the flow in this region, rupture of polymer chains has been reported [50]. Here, no chain rupture is predicted in the range of Deborah numbers considered.

In Fig. 9, the first normal-stress difference is plotted as a function of the radius of gyration for De = 7.0. Results show a very interesting stress-conformation hysteresis cycle, consistent with previous reports [1–3,6,7]. N_1 increases and attains a maximum around 19 units corresponding to a radius of gyration of 6.3σ at the contraction entry region and describes the hysteresis cycle downstream.

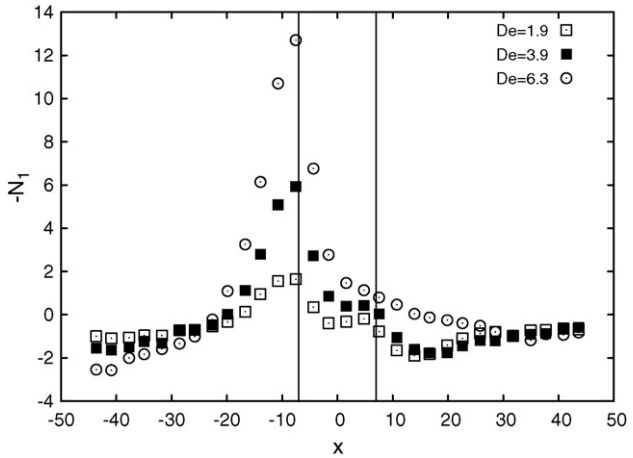

Fig. 6. First normal-stress difference along the central streamline for various Deborah numbers.

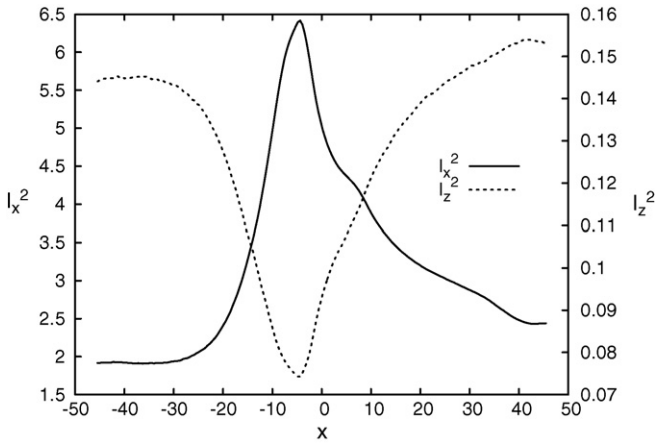

Fig. 8. Eigenvalues of the radius of gyration tensor I_x^2 and I_z^2 along the central streamline. De = 7.0.

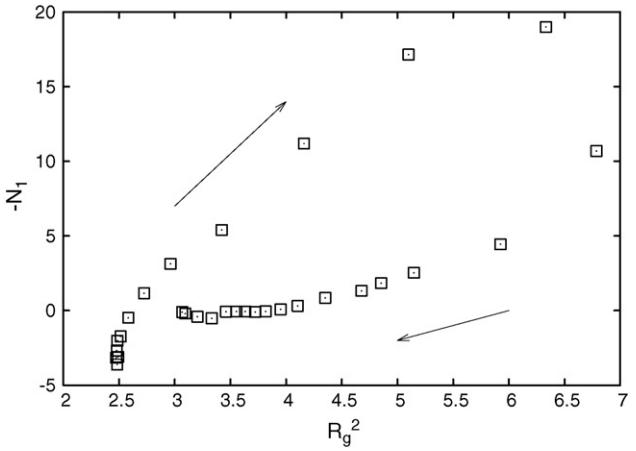

Fig. 9. First normal-stress difference as a function of the radius of gyration. De = 7.

4.3.2. Pressure drop

Results presented in this section support the assumption made on the relation between the excess in the pressure drop in viscoelastic fluids and the stress-deformation hysteresis cycles. As a most important prediction, it shows a remarkable increase of the pressure loss in the linear chains as compared to that of the Newtonian fluid. The pressure within the contraction–expansion test region depends on the T_{zz} component of the stress tensor. Calculations of this component is carried out through the MOP method allowing 100 planes x–y from the central streamline to the wall ($z = L_z/2$) prior and past the contraction. The area of each plane is $133.127\sigma^2$ and the separation between planes is 0.127σ. In Fig. 10a, the pressure gradient of linear molecules along the centerline of the geometry rises from the upstream constant value to a maximum, before decreasing to the expected same constant value downstream. The maximum pressure gradient increases with Deborah number. These predictions contrasts to those of Binding et al. [13] on contraction–expansion flows using an Oldroyd-B fluid, which predicts a decrease of the maximum pressure gradient with De number. In Fig. 10b, the normal-stress component T_{zz} is depicted for various trajectories away from the symmetry line for De = 7. The largest normal stress is found near $z = 0$ and close to the walls it presents a small peak at $-15\sigma < x < -10\sigma$ before diminishing. This

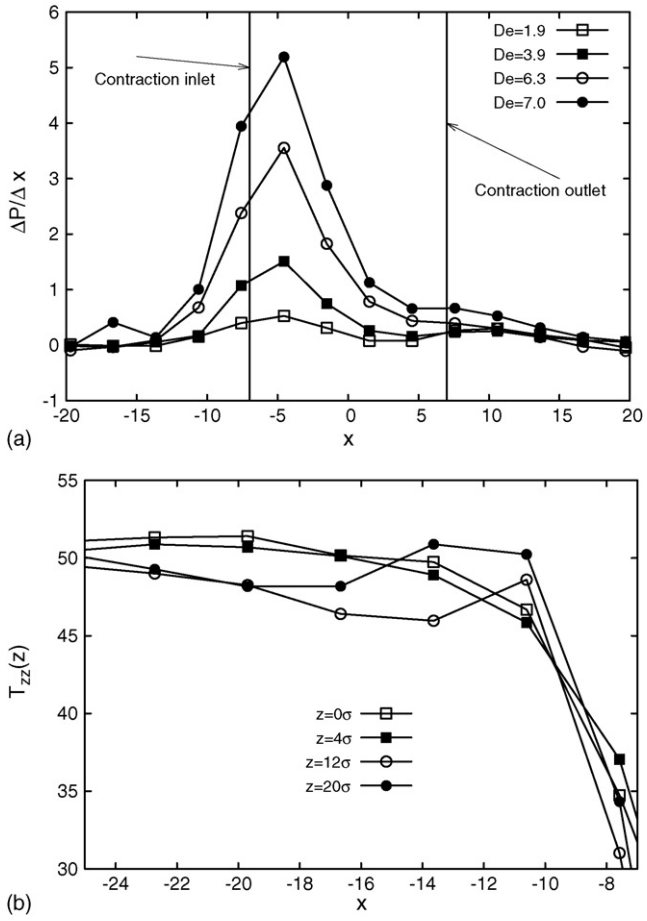

Fig. 10. (a) Centerline pressure gradient along the flow trajectory and (b) normal stress along flow trajectories parallel to the central streamline, De = 7.

increase is consistent with results obtained by Aguayo et al. [14] using continuum models, such as Oldroyd-B, Phan-Thien/Tanner and Pom-Pom, representing a Boger fluid.

Doyle et al. [1] found that the excess pressure drop is related to the energy dissipated along the stress-conformation hystere-

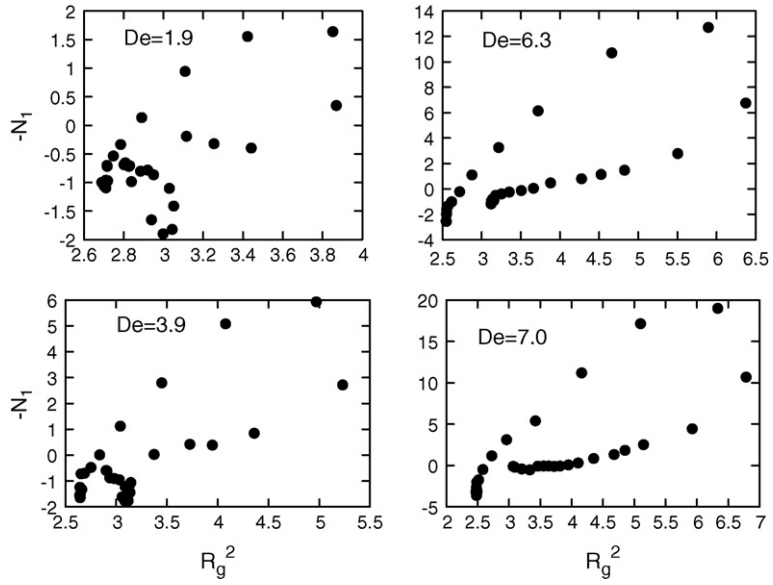

Fig. 11. Stress-conformation hysteresis cycles for various Deborah numbers.

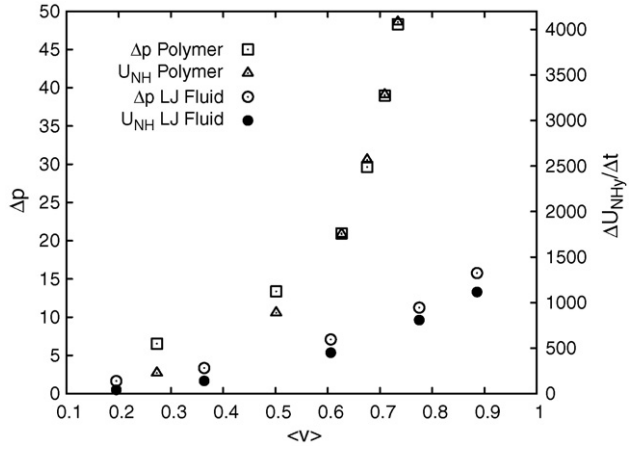

Fig. 12. Pressure drop and rate of dissipated energy as functions of the mean velocity for the polymer and Lennard–Jones fluid.

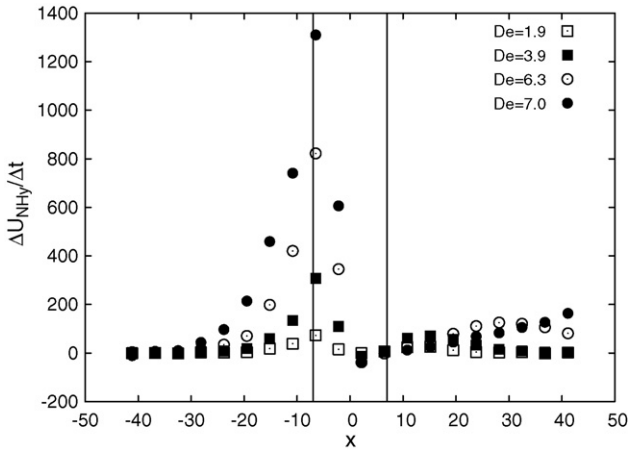

Fig. 13. Rate of dissipated energy of the molecules along the central streamline, for various Deborah numbers.

sis cycle. In Fig. 11 the stress-conformation hysteresis cycles as functions of Deborah number are presented. For De = 1.9, the hysteresis area is small, while for larger Deborah numbers the area of the hysteresis loop increases, as first normal-stress difference and radius of gyration augment. Rothstein and McKinley [7] suggest

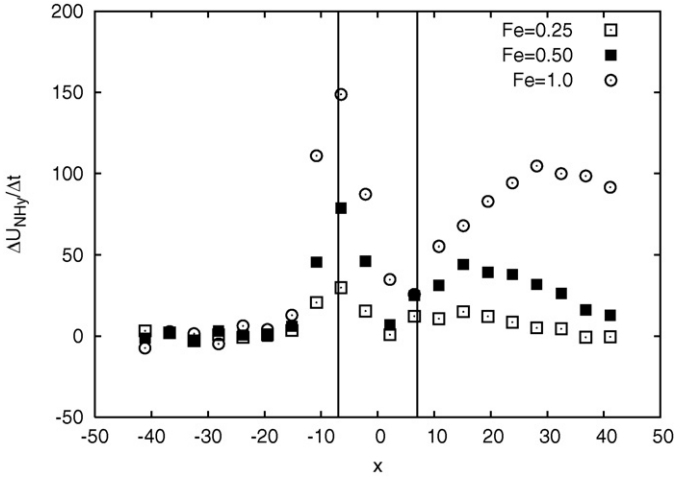

Fig. 14. Rate of dissipated energy of the Lennard–Jones fluid along the central streamline, for various values of the external force.

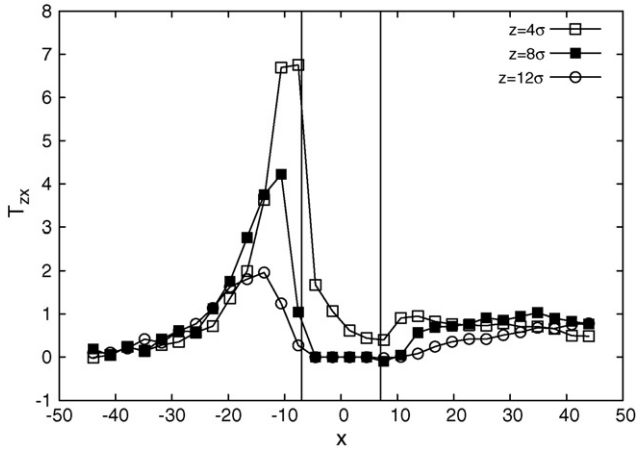

Fig. 15. Shear stress along the axial coordinate for various distances away from the central streamline, De = 6.3.

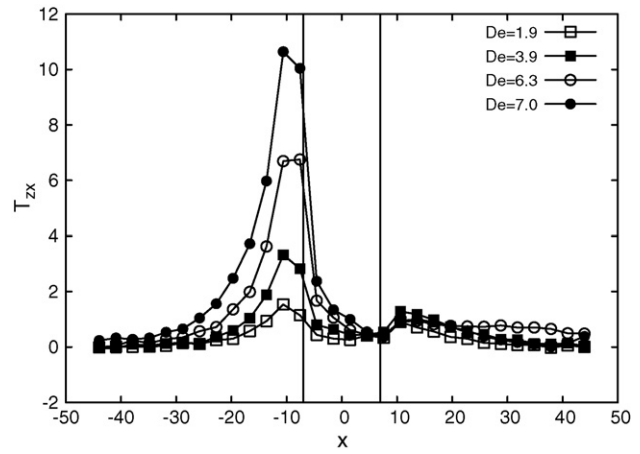

Fig. 16. Shear stress along the streamline located at $z = 4\sigma$ away from the central streamline, for various Deborah numbers.

that the area enclosed within the hysteresis loop represents the dissipated work per unit time of the coupling between stress and the extensional flow kinematics. Although in this work the rate of dissipated energy corresponds to the rate of energy removed by the thermostat, i.e., $E_v \approx \Delta U_{NH}/\Delta t$, to maintain a constant temperature, qualitative agreement with Ref. [7] is found.

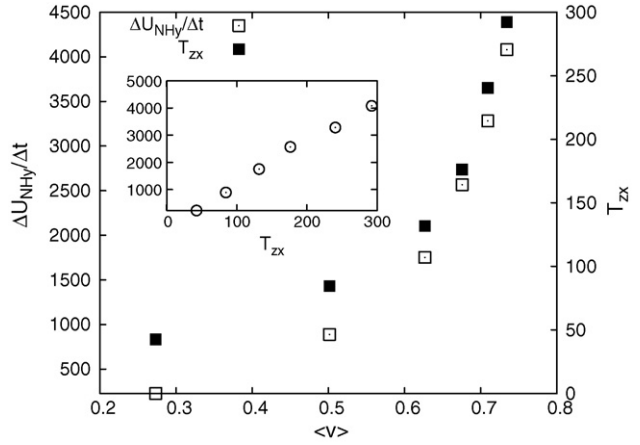

Fig. 17. Rate of dissipated energy and shear stress as functions of the mean velocity across the contraction–expansion geometry. Inset: rate of dissipated energy versus shear stress.

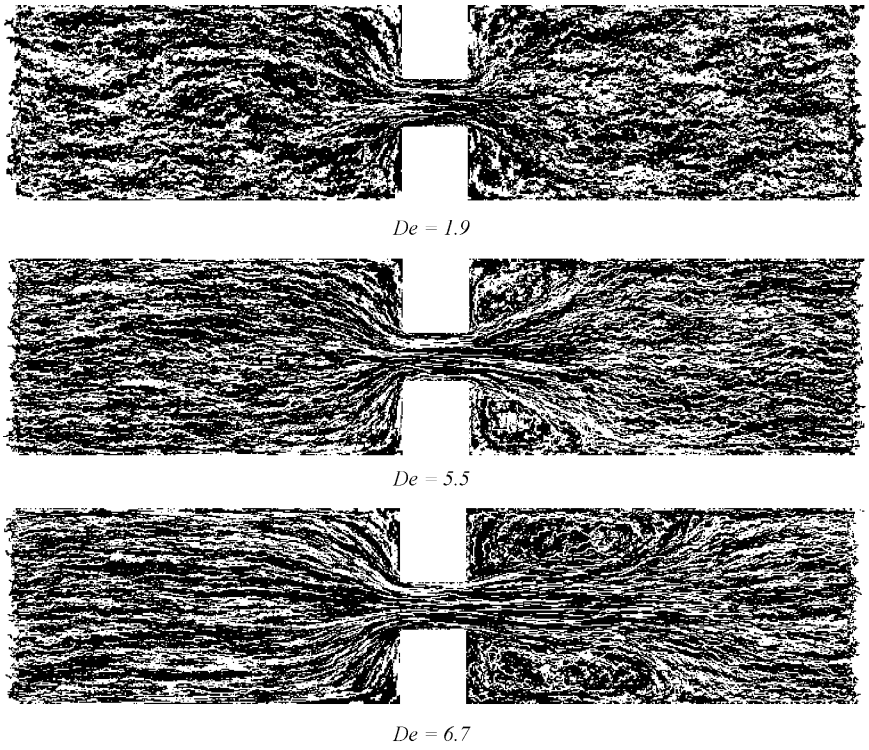

Fig. 18. History of the positions visited by the linear molecules for various Deborah numbers.

Fig. 12 shows results of the pressure drop $\Delta P = P_1 - P_2$ (P_2 and P_1 are the pressures past and prior the contraction) and $\Delta U_{NHy}/\Delta t$ as functions of the mean velocity $\langle v \rangle$ of the molecules and Lennard–Jones fluid across the contraction. The Lennard–Jones fluid pressure drop is linear for low values of the mean velocity, which contrasts with the drastic increase in the pressure drop exhibited by the polymer molecules. This is a remarkable prediction, since most constitutive equations do not predict such increase in the pressure drop as compared to Newtonian reference fluid, as shown here for the first time. Another important observation is that the pressure drop of both fluids can be related to the rate of energy removed by the thermostat, which is consistent with the fact that the pressure drop is proportional to the rate of dissipated energy.

Results presented in Fig. 12 reveal that the pressure drop exhibits a highly non-linear behavior for mean velocities larger than 0.62, corresponding to De = 5.5. Larger Deborah numbers imply higher magnitudes of dissipated energy and hence wider hysteresis loops. Likewise, the dissipated energy is associated to the work necessary to deform the polymer molecules as they enter the contraction region undergoing a relaxation-deformation-relaxation cycle.

Fig. 13 addresses the rate of energy removed by the thermostat for the polymer molecules along the flow direction in the test region. $\Delta U_{NHy}/\Delta t$ is close to zero up to $x \approx -30\sigma$ where it starts to grow up to a maximum located at the contraction entry length. This is consistent with the behavior along the geometry of the molecular deformation and pressure drop predictions. In all cases, as the De number increases, the rate of dissipated energy also augments. In the contraction region, $\Delta U_{NHy}/\Delta t$ diminishes and further in the expansion region according to the relaxation process of the molecules. In the case of the Lennard–Jones fluid, in Fig. 14 similar results are obtained as pressure gradient increases, except that the magnitudes are one decade lower than those of the polymer molecules.

The rate of energy removed by the thermostat is related to the shear stress along the test region. In Fig. 15 the shear stress T_{zx} of molecules is plotted with the axial coordinate along three planes located normal to $z = 4, 8$ and 12σ for De = 6.3. The trajectories along which the stress is calculated show the influence of the corner on the shear stress. The largest shear stress is found prior to the contraction in the region $-15\sigma < x < -6.9$, ascribed to the plane $z = 4\sigma$, corresponding to the trajectory that is closer to the corners. In Fig. 16, the shear stress as a function of the Deborah number is depicted for $z = 4\sigma$, showing the increase in the shear stress with the Deborah number near the corners. In Fig. 17 the shear stress of the system with linear molecules and the rate of energy removed by the thermostat are plotted with the mean velocity at the entry region of the contraction, within the test region. This figure clearly shows the close relationship existing between the shear stress and the rate of removed energy, and hence with the pressure loss.

Finally, Fig. 18 describes the history of positions visited by the linear-chain molecules for various Deborah numbers. The presence of vortices at the exit of the contraction is related to the value of the Deborah number. This behavior bears similarities to that found in the flow of linear-chain polystyrenes through a contraction–expansion device [51].

5. Conclusions

Results on the simulation of the viscoelastic flow (through a 4:1:4 contraction–expansion geometry) of linear chains modeled with a FENE potential and a Lennard–Jones fluid by non-equilibrium molecular dynamics lead to the following conclusions:

- The flow velocity increase prior the contraction is a function of the Deborah number, and its maximum shifts downstream for increasing De numbers. The strain rate, consequently, presents two main peaks: one located just before the contraction, and a second one of negative sign in the expansion region.
- The extensional component of the stress also attains its maximum just before the contraction, and increases in magnitude with the De number.

- The molecular deformation, i.e., the radius of gyration, presents a maximum just after the contraction line, undergoing a relaxation in the contraction itself. The magnitude of the peaks increases with De number.
- The behavior of N_1 is consistent with the conformation changes of the molecule along the flow direction. The chain segments are extended along the flow direction and compressed in the normal direction (see Figs. 7 and 8).
- Results show the presence of stress-conformation hysteresis cycles, i.e., the normal stress and the radius of gyration evolve following a specific path during deformation and a different path during the relaxation process. The area enclosed within the cycles increases with the De number.
- The most important result is the theoretical prediction, to our knowledge shown here in this general context for the first time, of a remarkable increase of the pressure loss in the polymer fluid, one order of magnitude larger than that predicted for the Lennard–Jones Newtonian fluid. Moreover, a second important contribution is the description of the close relationship existing between the pressure drop and the dissipated energy through the contraction. In this regard, the rate of dissipated energy can be directly related to the area of the hysteresis loops and with the shear stress.
- Specifically, the region next to the contraction is that where larger rates of dissipated energy occur, and that where the largest pressure drop is predicted, corresponding to the largest area of the hysteresis cycles. The shear stress follows a linear relation with the rate of dissipated energy and a maximum is predicted near the corner regions.

Acknowledgement

The authors are grateful for the financial support from the Consejo Nacional de Ciencia y Tecnología (CONACYT) through the projects 47192 and 83501.

References

[1] P.S. Doyle, E.S.G. Shaqfeh, G.H. McKinley, S.H. Spiegelberg, Relaxation of dilute polymer solutions following extensional flow, J. Non-Newtonian Fluid Mech. 76 (1998) 79–110.
[2] G. Lielens, P. Halin, I. Jaumain, R. Keunings, V. Legat, New closure approximations for the kinetic theory of finitely extensible dumbbells, J. Non-Newtonian Fluid Mech. 76 (1998) 249–279.
[3] R. Sizaire, G. Lielens, I. Jaumain, R. Keunings, V. Legat, On the hysteretic behaviour of dilute polymer solutions in relaxation following extensional flow, J. Non-Newtonian Fluid Mech. 82 (1999) 233–253.
[4] J.P. Rothstein, G.H. McKinley, Extensional flow of a polystyrene Boger fluid through a 4:1:4 axisymmetric contraction/expansion, J. Non-Newtonian Fluid Mech. 86 (1999) 61–88.
[5] J.P. Rothstein, G.H. McKinley, The axisymmetric contraction–expansion: the role of extensional rheology on vortex growth dynamics and the enhanced pressure drop, J. Non-Newtonian Fluid Mech. 98 (2001) 33–63.
[6] J.P. Rothstein, G.H. McKinley, A comparison of the stress and birefringence growth of dilute, semi-dilute and concentrated polymer solutions in uniaxial extensional flows, J. Non-Newtonian Fluid Mech. 108 (2002) 275–290.
[7] J.P. Rothstein, G.H. McKinley, Inhomogeneous transient uniaxial extensional rheometry, J. Rheol. 46 (2002) 1419–1443.
[8] S. Nigen, K. Walters, Viscoelastic contraction flows: comparison of axisymmetric and planar configurations, J. Non-Newtonian Fluid Mech. 102 (2002) 343–359.
[9] C.H. Schroeder, H.P. Babcock, E.S.G. Shaqfeh, S. Chu, Observation of polymer conformation hysteresis in extensional flow, Science 301 (2003) 1515–1519.
[10] P. Szabo, J.M. Rallison, E.J. Hinch, Start-up of flow of a FENE-fluid through a 4:1:4 constriction in a tube, J. Non-Newtonian Fluid Mech. 72 (1997) 73–86.
[11] K.D. Knudsen, J.G. Hernández Cifre, J. García de la Torre, Conformation and fracture of polystyrene chains in extensional flow studied by numerical simulation, Macromolecules 29 (1996) 3603–3610.
[12] S. Xue, N. Phan-Thien, R.I. Tanner, Numerical investigations of Lagrangian unsteady extensional flows of viscoelastic fluids in 3D rectangular ducts with sudden contractions, Rheol. Acta 37 (1998) 158–169.
[13] D.M. Binding, P.M. Phillips, T.N. Phillips, Contraction/expansion flows: the pressure drop and related issues, J. Non-Newtonian Fluid Mech. 137 (2006) 31–38.
[14] J.P. Aguayo, H.R. Tamaddon-Jahromi, M.F. Webster, Excess pressure-drop estimation in contraction and expansion flows for constant shear-viscosity, extension strain-hardening fluids, J. Non-Newtonian Fluid Mech. 153 (2008) 157–176.
[15] P. Wapperom, R. Keunings, Numerical simulation of branched polymer melts in transient complex flow using Pom-Pom models, J. Non-Newtonian Fluid Mech. 97 (2001) 267–281.
[16] T.C.B. McLeish, R.G. Larson, Molecular constitutive equations for a class of branched polymers: The Pom-Pom polymer, J. Rheol. 42 (1998) 81–110.
[17] R.J. Blackwell, T.C.B. McLeish, O.G. Harlen, Molecular drag-strain coupling in branched polymer melts, J. Rheol. 44 (2000) 121–136.
[18] M.A. Alves, P.J. Oliveira, F.T. Pinho, Benchmark solutions for the flow of Oldroyd-B and PTT fluids in planar contractions, J. Non-Newtonian Fluid Mech. 110 (2003) 45–75.
[19] M.A. Alves, F.T. Pinho, P.J. Oliveira, Visualizations of Boger fluid flows in a 4:1 square–square contraction, AIChE J. 51 (2005) 2908–2922.
[20] J.M. Kim, C. Kim, J.H. Kim, C. Cheng, K.H. Ahn, S.J. Lee, High-resolution finite element simulation of 4:1 planar contraction flow of viscoelastic fluid, J. Non-Newtonian Fluid Mech. 129 (2005) 23–37.
[21] Y. Kwon, Finite element analysis of planar 4:1 contraction flow with the tensor-logarithmic formulation of differential constitutive equations, Korea–Aust. Rheol. J. 16 (2004) 183–191.
[22] J. Ramirez, M. Laso, Micro–macro simulations of three-dimensional plane contraction flow, Model. Simul. Mater. Sci. Eng. 12 (2004) 1293–1306.
[23] S. Yoon, Y. Kwon, Finite element analysis of viscoelastic flows in a domain with geometric singularities, Korea–Aust. Rheol. J. 17 (2005) 99–110.
[24] R.B. Bird, R.C. Armstrong, O. Hassager, Dynamics of Polymeric Liquids: Volume II Kinetic Theory, John Wiley & Sons, 1987.
[25] B. Todd, D. Evans, P. Daivis, Pressure tensor for inhomogeneous fluids, Phys. Rev. E 52 (1995) 1627–1638.
[26] X. Mi, A. Chwang, Molecular dynamics simulations of nanochannel flows at low Reynolds numbers, Molecules 8 (2003) 193–206.
[27] J. Castillo-Tejas, J.F.J. Alvarado, G. González-Alatorre, G. Luna-Barcenas, I.C. Sanchez, R. Macias-Salinas, O. Manero, Non-equilibrium molecular dynamics of the rheological and structural properties of linear and branched molecules. Simple shear and Poiseuille flows; instabilities and slip, J. Chem. Phys. 123 (054907) (2005) 1–15.
[28] B.D. Todd, P.J. Daivis, Elongational viscosities from nonequilibrium molecular dynamics simulations of oscillatory elongational flow, J. Chem. Phys. 107 (1997) 1617–1624.
[29] B.D. Todd, P.J. Daivis, Nonequilibrium molecular dynamics simulations of planar elongational flow with spatially and temporally periodic boundary conditions, Phys. Rev. Lett. 81 (1998) 1118–1121.
[30] D. Evans, G. Morriss, Statistical Mechanics of Non-equilibrium Liquids, Academic Press, New York, 1990.
[31] S. Nose, A unified formulation of the constant temperature molecular dynamics methods, J. Chem. Phys. 81 (1984) 511–519.
[32] M. Tuckerman, B.J. Berne, G.J. Martyna, Reversible multiple time scale molecular dynamics, J. Chem. Phys. 97 (1992) 1990–2001.
[33] G.J. Martyna, M.E. Tuckerman, D.J. Tobias, M.L. Klein, Explicit reversible integrators for extended systems dynamics, Mol. Phys. 87 (1996) 1117–1157.
[34] Z. Xu, J. de Pablo, S. Kim, Transport properties of polymer melts from non-equilibrium molecular dynamics, J. Chem. Phys. 102 (1995) 5836–5844.
[35] K. Kremer, G. Grest, Dynamics of entangled linear polymer melts: a molecular-dynamics simulation, J. Chem. Phys. 92 (1990) 5057–5086.
[36] J.D. Weeks, D. Chandler, H.C. Andersen, Role of repulsive forces in determining the equilibrium structure of simple liquids, J. Chem. Phys. 54 (1971) 5237–5247.
[37] H.R. Warner Jr., Kinetic theory and rheology of dilute suspensions of finitely extensible dumbbells, Ind. Eng. Chem. Fund. 11 (1972) 379–387.
[38] R. Bird, C. Curtiss, R. Armstrong, O. Hassager, Dynamics of Polymeric Liquids: Volume 2 Kinetic Theory, Wiley, New York, 1987.
[39] R. Khare, J. de Pablo, A. Yethiraj, Rheology of confined polymer melts, Macromolecules 29 (1996) 7910–7918.
[40] T. Aoyagi, J. Takimoto, M. Doi, Molecular dynamics study of polymer melt confined between walls, J. Chem. Phys. 115 (2001) 552–559.
[41] R.B. Pandey, A. Milchev, K. Binder, Semi-dilute and concentrated polymer solutions near attractive walls: dynamic Monte Carlo simulation of density and pressure profiles of a coarse-grained model, Macromolecules 30 (1997) 1194–1204.
[42] J.A. Pryde, The Liquid State, Hutchinson University Library, London, 1969.
[43] M.P. Allen, D.J. Tildesley, Computer Simulation of Liquids, Clarendon Press, Oxford, 1987.
[44] F. Varnik, J. Baschnagel, K. Binder, Molecular dynamics results on the pressure tensor of polymer films, J. Chem. Phys. 113 (2000) 4444–4453.
[45] A.W. Lees, S.F. Edwards, The computer study of transport processes under extreme conditions, J. Phys. C 5 (1972) 1921–1928.
[46] R. Bird, R. Armstrong, O. Hassager, Dynamics of Polymeric Liquids: Volume I Fluid Mechanics, Wiley, New York, 1987.
[47] R.B. Bird, W.E. Stewart, E.N. Lightfoot, Transport Phenomena, John Wiley & Sons, Inc., 2002.

[48] J.M. Haile, Molecular Dynamics Simulation: Elementary Methods, John Wiley & Sons, New York, 1997.
[49] R.S. Graham, J. Bent, L.R. Hutchings, R.W. Richards, D.J. Groves, J. Embery, T.M. Nicholson, T.C.B. McLeish, A.E. Likhtman, O.G. Harlen, D.J. Read, T. Gough, R. Spares, P.D. Coates, I. Grillo, Measuring and predicting the dynamics of linear monodisperse entangled polymers in rapid flow through an abrupt contraction. A small- angle neutron-scattering study, Macromolecules 39 (2006) 2700–2709.
[50] J.D. Clay, K.W. Koelling, Molecular degradation of concentrated polystyrene solutions in a fast transient extensional flow, Polym. Eng. Sci. 37 (1997) 789–800.
[51] G.B. Bishko, O.G. Harlen, T.C.B. McLeish, T.M. Nicholson, Numerical simulation of the transient flow of branched polymer melts through a planar contraction using the Pom–Pom model, J. Non-Newtonian Fluid Mech. 82 (1999) 255–273.